

# Experimental demonstration of the dynamics of quantum coherence evolving under a PT-symmetric Hamiltonian on an NMR quantum processor

Akanksha Gautam\* and Kavita Dorai†

*Department of Physical Sciences, Indian Institute of Science Education & Research Mohali,  
Sector 81 SAS Nagar, Manauli PO 140306 Punjab India.*

Arvind‡

*Department of Physical Sciences, Indian Institute of Science Education & Research Mohali,  
Sector 81 SAS Nagar, Manauli PO 140306 Punjab India. and  
Vice Chancellor, Punjabi University Patiala, 147002, Punjab, India*

In this work, we study the dynamics of quantum coherence (total coherence, global coherence and local coherence) evolving under a local PT-symmetric Hamiltonian in maximally entangled bipartite and tripartite states. Our results indicate that quantum coherence in the bipartite state oscillates in the unbroken phase regime of the PT-symmetric Hamiltonian. Interestingly, in the broken phase regime, while the global coherence decays exponentially, the local and total coherences enter a “freezing” regime where they attain a stable value over time. A similar pattern is observed for the dynamics of total and local coherences in the maximally entangled tripartite state, while the dynamics of global coherence in this state differs from that of the bipartite state. These results were experimentally validated for a maximally entangled bipartite state on a three-qubit nuclear magnetic resonance (NMR) quantum processor, with one of the qubits acting as an ancilla. The experimental results match well with the theoretical predictions, upto experimental errors.

## I. INTRODUCTION

The hermiticity of physical observables in standard quantum mechanics ensures both real energy spectra of quantum systems and unitary evolution of closed systems. In 1998, Bender and Boettcher discovered certain parity-time (PT) symmetric Hamiltonians that despite being non-hermitian, can still have real energy spectra, thereby demonstrating that hermiticity is a sufficient condition but not necessary [1, 2]. It was observed that the eigenvalues of the PT-symmetric Hamiltonian are always real and PT-symmetry is unbroken if the eigenstates of a PT-symmetric Hamiltonian are also eigenstates of the PT operator; otherwise, the eigenvalues are complex and PT-symmetry is broken. The point where the eigenvalues and eigenvectors coalesce, causing a transition from unbroken to broken PT-symmetry is called the exceptional point [3, 4].

PT-symmetric Hamiltonians have been implemented on various experimental platforms including ultracold atoms [5], superconducting circuits [6, 7], nitrogen-vacancy centers in diamonds [8, 9], optical waveguides [10, 11] and NMR spins [12]. The anti-PT-symmetric Hamiltonian was implemented using NMR spins where information flow between the system and environment was experimentally explored [13].

PT-symmetric Hamiltonians have attracted wide attention due to their interesting features, and numerous studies have been performed including increase or

restoration of entanglement by a local PT-symmetric Hamiltonian [12, 14], protecting quantum correlations via non-hermitian operations [15], no-signaling principle violation [16, 17], observing fast evolution in a PT-symmetric system [18, 19] and observing critical phenomena in a PT-symmetric system [20, 21]. Recently, it has been shown that quantum coherence is increased in a single-qubit system under PT-symmetric Hamiltonian and maximal quantum coherence is observed at the exceptional point [22, 23]. The flow of quantum coherence of a single qubit under PT-symmetric and anti-PT-symmetric Hamiltonians has been demonstrated on an optics system [24].

Different measures of basis dependent quantum coherence have been proposed such as  $l_1$ -norm and relative entropy [33, 36–38]. Based on these measures, various types of quantum coherences have been defined in multipartite systems such as global coherence, local coherence and total coherence [39, 40]. Recently, bipartite and tripartite entanglement has been generated in a PT-symmetric system that involves three interacting cavities [34]. The evolution process of entropy and entanglement in a three-qubit system has been investigated using nuclear spins [35].

In this work, we use the relative entropy of coherence [33] to quantify quantum coherence of various kinds present in a multipartite system, and explicitly study their dynamics in a bipartite and a tripartite system evolving under a local PT-symmetric Hamiltonian. In the maximally entangled bipartite (Bell) and tripartite (GHZ) states, only global coherence exists while local coherence remains zero. Our theoretical results show that local coherence, which previously did not exist in such maximally entangled states, gets created under the local PT-symmetric Hamiltonian. Global, local and total

\* akankshagautam@iisermohali.ac.in

† kavita@iisermohali.ac.in

‡ arvind@iisermohali.ac.in

coherences in the bipartite entangled state show an oscillatory behavior in the unbroken PT-symmetry regime. On the other hand, in the broken PT-symmetry regime, global coherence first increases then decays exponentially; total coherence also increases initially but attains a stable value at later times, while local coherence is first created, then increases and stabilizes at later times. Similar patterns of coherence dynamics is observed in the tripartite maximally entangled state, in the unbroken regime of PT-symmetry. In the broken phase of PT-symmetry, the pattern of total and local coherences are similar to the bipartite state but the global coherence exhibits a different dynamics. Further, the dynamics of quantum coherence present in a two-qubit reduced state of a tripartite state was investigated under the PT-symmetric Hamiltonian in both unbroken and broken phase regimes. We have also experimentally demonstrated the dynamics of quantum coherence of a maximally entangled bipartite state using three NMR qubits. Two of the qubits were utilized to prepare two-qubit states and the third qubit was used as an ancillary qubit to simulate a PT-symmetric Hamiltonian acting on one of the qubits. Both broken as well as unbroken phase regimes of the PT-symmetric Hamiltonian were simulated experimentally and the dynamics of various types of quantum coherences in the maximally entangled bipartite state was verified.

This article is organized as follows: Section II describes the procedure to simulate a general PT-symmetric Hamiltonian. Section III contains details of the simulation of the dynamics of quantum coherence (global coherence, local coherence and total coherence) in a maximally entangled bipartite (Bell) state and a tripartite (GHZ) state evolving under the local PT-symmetric Hamiltonian. Section IV contains the experimental results of the implementation of the local PT-symmetric Hamiltonian on a maximally entangled bipartite state. Section V contains some concluding remarks.

## II. SIMULATION OF THE PT-SYMMETRIC HAMILTONIAN

While all hermitian Hamiltonians can be realized by unitary operations, the PT-symmetric Hamiltonian (being non-hermitian) can cause non-unitary evolution and is hence nontrivial to simulate on a quantum processor. The PT-symmetric Hamiltonian can be simulated by enlarging the system into a higher-dimensional Hilbert space by using an ancillary qubit. The PT-symmetric Hamiltonian for a single qubit can be written as [2]:

$$H_{PT} = \sigma_x + ir\sigma_z \quad (1)$$

where  $r > 0$  is the amount of non-hermiticity and  $\sigma_x, \sigma_y, \sigma_z$  are Pauli matrices. The PT-symmetric Hamiltonian satisfies the condition  $(PT)H^\dagger(PT)^{-1} = H$ , where  $P = \sigma_x$  is the parity operator and  $T$  denotes the complex conjugation operator. The energy gap  $g$  of

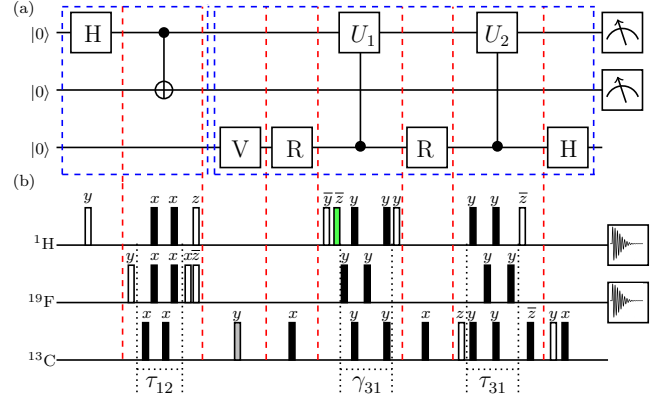


FIG. 1. (a) Quantum circuit to simulate a PT-symmetric Hamiltonian. The gates in the first box create a maximally entangled Bell state ( $\rho_{BS} \otimes \rho_0$ ) on the first two qubits, with the third qubit acting as an ancillary qubit. The action of the  $V$ ,  $U_1$  and  $U_2$  gates is described in the main text.  $H$  is a Hadamard gate and  $R$  acts as a NOT gate when  $\phi$  (given in Eq.7) is negative, otherwise  $R$  is an  $I_2$  identity operation. (b) The corresponding NMR pulse sequence, where the unfilled rectangles are  $\frac{\pi}{2}$  pulses, the black rectangles denote  $\pi$  pulses, the grey rectangle is a  $\theta$  pulse and the green rectangle denotes a  $\phi$  pulse. Pulse phases are given above each pulse and a bar over a phase represents negative phase. The free evolution time intervals  $\tau_{12}$  and  $\tau_{31}$  are given by  $1/2J_{12}$  and  $1/2J_{31}$  respectively, where  $J_{12}$  and  $J_{31}$  are scalar coupling constants.

the PT-symmetric Hamiltonian is  $g = 2\sqrt{1-r^2}$  and its eigenvalues are  $\pm\sqrt{1-r^2}$ ; for  $|r| < 1$  the eigenvalues are positive, which means that the PT-symmetry is unbroken and for  $|r| > 1$  the eigenvalues become complex, which leads to a broken PT-symmetry. The Hamiltonian has an exceptional point at  $|r| = 1$ , where both the eigenvalues as well as the eigenvectors coalesce.

The evolution of  $H_{PT}$  can be realized by introducing an ancillary qubit to simulate the non-unitary operator  $U_{PT} = e^{-iH_{PT}t}$ , where  $t$  represents evolution time and the matrix form of the local operation  $U_{PT} = e^{-iH_{PT}t}$  is represented by

$$U_{PT} = \begin{bmatrix} \cos \omega t - \frac{ir \sin \omega t}{\omega} & -\frac{i \sin \omega t}{\omega} \\ -\frac{i \sin \omega t}{\omega} & \cos \omega t + \frac{ir \sin \omega t}{\omega} \end{bmatrix} \quad (2)$$

where  $\omega = \sqrt{1+r^2}$ . Thus, this non-unitary operator can be implemented by a linear combination of unitary operators using an ancillary qubit [12, 41, 42] and the quantum circuit to implement it is shown in Fig.1(a), where the initial state  $|\psi\rangle|0\rangle$  is first created. Then the unitary operator  $V$  is performed on ancillary qubit which is represented as [12]:

$$V = \begin{bmatrix} \cos \theta & -\sin \theta \\ \sin \theta & \cos \theta \end{bmatrix} \quad (3)$$

where

$$\cos \theta = \sqrt{\frac{1-r^2 \cos^2 gt/2}{1-r^2 \cos gt}}, \sin \theta = \frac{r \sin gt/2}{\sqrt{1-r^2 \cos gt}} \quad (4)$$

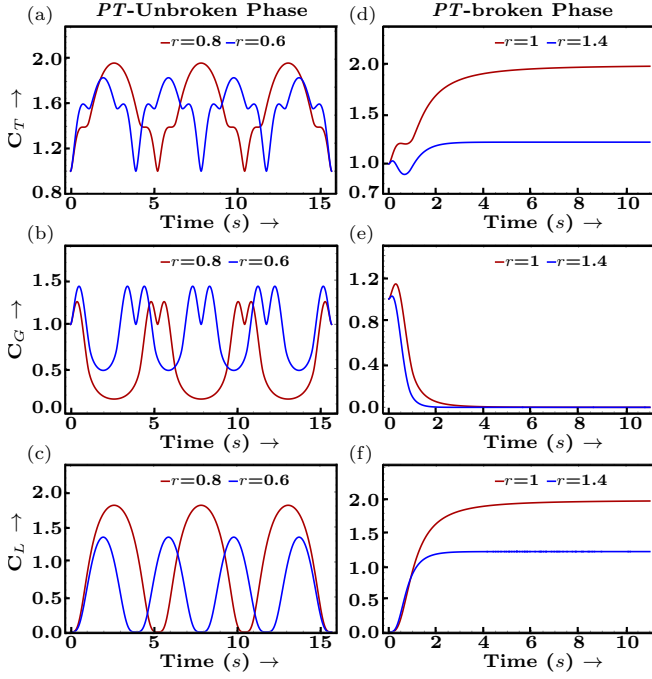


FIG. 2. Plots of the evolution of quantum coherence present in the maximally entangled bipartite (Bell) state under different phases of PT-symmetry. (a), (b) and (c) represent the dynamics of total coherence ( $C_T$ ), global coherence ( $C_G$ ) and local coherence ( $C_L$ ) respectively, in the unbroken phase (at  $r = 0.6$  and  $r = 0.8$ ). (d), (e) and (f) represent the dynamics of total, global and local coherence respectively, in the broken phase (at  $r = 1.4$  and at exceptional point  $r = 1$ ).

The two controlled unitary operations  $C_{U_1}$  and  $C_{U_2}$  are then performed on the first qubit of the two-qubit work state using the ancillary qubit and the matrix form of these operations are represented by [12]:

$$C_{U_1} = \begin{bmatrix} U_1 & 0 \\ 0 & I \end{bmatrix} \quad C_{U_2} = \begin{bmatrix} I & 0 \\ 0 & U_2 \end{bmatrix} \quad (5)$$

where

$$U_1 = \begin{bmatrix} \cos \phi & i \sin \phi \\ i \sin \phi & \cos \phi \end{bmatrix} \quad U_2 = \sigma_z \quad (6)$$

and

$$\cos \phi = \frac{g \cos gt/2}{2\sqrt{1-r^2 \cos^2 gt/2}}, \sin \phi = \frac{-r \sin gt/2}{\sqrt{1-r^2 \cos^2 gt/2}} \quad (7)$$

and the last operation is a Hadamard gate on the ancillary qubit. The state is then measured in the subspace spanned by  $|0\rangle$  of the ancillary qubit, which leads to the final state where the local PT-symmetric Hamiltonian has been implemented.

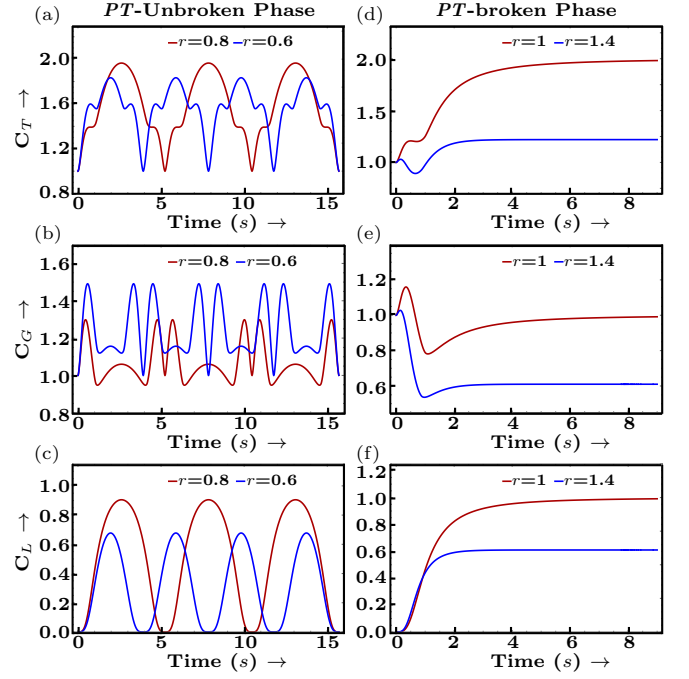


FIG. 3. Plots of the evolution of quantum coherence present in a maximally entangled tripartite (GHZ) state under different phases of PT-symmetry. (a), (b) and (c) represent the dynamics of total coherence ( $C_T$ ), global coherence ( $C_G$ ) and local coherence ( $C_L$ ) respectively, in the unbroken phase (at  $r = 0.6$  and  $r = 0.8$ ). (d), (e) and (f) represent the dynamics of total, global and local coherence respectively, in the broken phase (at  $r = 1.4$  and at exceptional point  $r = 1$ ).

### III. DYNAMICS OF QUANTUM COHERENCE UNDER THE PT-SYMMETRIC HAMILTONIAN

#### A. Measures of quantum coherence

Several measures have been proposed to quantify quantum coherence that follow certain properties such as relative entropy and  $l_1$  norm [33]. These measures have further been utilized to quantify different types of quantum coherences present in multipartite systems such as total coherence, local coherence and global coherence which are described below [39, 40].

*Total quantum coherence-* The total quantum coherence [33] of the system is defined as the measure of its distance to the closest incoherent state, where the incoherent state has the form  $\sigma = \sum_i p_i |i\rangle\langle i|$  and the fixed local basis  $\{|i\rangle\}$  for each qubit is  $\{|0\rangle, |1\rangle\}$ . The relative entropy of coherence is defined as [33]:

$$C_T(\rho) = \min_{\sigma \in I} S(\rho \| \sigma) = S(\rho_d) - S(\rho) \quad (8)$$

where  $S(\rho) = -\text{tr}(\rho \log_2 \rho)$  is the Von-Neumann entropy of  $\rho$ , and  $\rho_d$  is the matrix of  $\rho$  with all off-diagonal terms set to zero in the basis  $|i\rangle$ .

*Local coherence-* Quantum coherence which is localized

on each qubit of the entire system is called local coherence [39, 40]. For example, in a separable two-qubit state  $|+-\rangle = (|0\rangle + |1\rangle)(|0\rangle - |1\rangle)/2$ , quantum coherence exists in each qubit. Local coherence can also be defined in terms of the relative entropy [39, 40]:

$$C_L(\rho) = \min_{\sigma \in \mathcal{L}} S(\delta(\rho) \parallel \sigma) = S(\delta_d(\rho)) - S(\delta(\rho)) \quad (9)$$

where  $\delta(\rho) = \rho_1 \otimes \rho_2$  ( $\delta(\rho) = \rho_1 \otimes \rho_2 \otimes \rho_3$ ) for a two-qubit state (three-qubit state) and  $\rho_1 = \text{Tr}_2 \rho_{12}$  ( $\rho_1 = \text{Tr}_{23} \rho_{123}$ ) is the single-qubit reduced density matrix;  $\delta_d(\rho)$  is the matrix produced by eliminating all off-diagonal elements of  $\delta(\rho)$  in the basis  $|i\rangle$ .

*Global Coherence*- Quantum coherence that originates due to the collective nature of the whole system is called global coherence [39, 40]. Mathematically, it is the difference between total quantum coherence and local coherence [39, 40]:

$$C_G(\rho) = C_T(\rho) - C_L(\rho) \quad (10)$$

### B. Two-qubit maximally entangled (Bell) state

Consider a two-qubit Bell state defined as

$$\begin{aligned} \rho_{BS} &= |\psi_{BS}\rangle\langle\psi_{BS}| \quad \text{with} \\ |\psi_{BS}\rangle &= \frac{1}{\sqrt{2}}(|00\rangle + |11\rangle) \end{aligned} \quad (11)$$

Our aim is to study the dynamics of various types of quantum coherences, namely the total, global and local coherence as the state evolves from  $\rho_{BS}$  under the local operation generated by the PT-symmetric non-hermitian Hamiltonian [2] (Eq.(1)), acting on one of the qubits. The final density matrix after the action of  $U_{PT}^2 = U_{PT} \otimes I$  on the initial state  $\rho_{BS}$  is given by:

$$\rho_{BS}(t) = \frac{U_{PT}^2 \rho_{BS}(0) U_{PT}^2}{\text{Tr}[U_{PT}^2 \rho_{BS}(0) U_{PT}^2]} \quad (12)$$

From this state, we calculate the total, global and local coherence by using the definitions given in Eqs. 8,9 and 10, respectively. The regions of interest are the broken and unbroken phase regimes of the PT-symmetric Hamiltonian and the exceptional point [2].

The results of these calculations for the unbroken and broken PT-symmetry regimes are plotted in Fig. 2. Figs. 2(a)-(c) contain the plots of the total, global and local coherence as a function of time for the unbroken PT-symmetry regime, while Figs. 2(d)-(f) contain the same for the broken PT-symmetry regime. It can be observed from Fig.2(a)-(c) that all the different types of coherences (total, global and local coherence) show an oscillatory behavior for the unbroken PT-symmetry regime. The amplitude of the total and local coherence increases as the parameter  $r$  approaches to  $r = 1$  (exceptional point), while the amplitude of global coherence decreases as the parameter  $r$  approaches the exceptional

point. The transition in the dynamics of quantum coherence once the exceptional point is reached, can be observed in Figs.2(d)-(f), where the amplitude of total quantum coherence initially increases and then freezes at later times. A similar behavior is observed in the dynamics of local coherence in the broken phase regime (which is initially absent and is created when acted upon by the PT-symmetric Hamiltonian) where its amplitude first increases and then attains a stable value. The freezing behavior of quantum coherence depicted in Fig. 2 is different from the dynamics of previously observed quantum correlations (both entanglement and quantum discord) in the maximally entangled state in the broken phase. The global coherence in the broken phase of PT-symmetry first increases with time and then decays exponentially to zero. The discussion of the dynamics of various coherences at the exceptional point ( $r = 1$ ) will be taken up later in Section III D.

### C. Three-qubit maximally entangled state (GHZ state)

Next we consider three-qubit states and analyze the evolution of their coherence properties when one of the qubits is subjected to time evolution generated by the PT-symmetric Hamiltonian (Eq. (1)). We first consider the maximally entangled Greenberger-Horne-Zeilinger (GHZ) state:

$$\begin{aligned} \rho_{GHZ} &= |\psi_{GHZ}\rangle\langle\psi_{GHZ}| \quad \text{where} \\ |\psi_{GHZ}\rangle &= \frac{1}{\sqrt{2}}(|000\rangle + |111\rangle) \end{aligned} \quad (13)$$

Taking the GHZ state as the initial state, we consider the action of the PT-symmetric Hamiltonian (Eq. (1)) on the first qubit. This amounts to evaluating the action of the operator  $U_{PT}$  defined in Eq. (2) on the first qubit, leading to the overall operation on the three-qubit system to be implemented as:

$$U_{PT}^3 = U_{PT} \otimes I \otimes I. \quad (14)$$

The final normalized density operator corresponding to the local action of the PT-symmetric Hamiltonian on the GHZ state then can be written as:

$$\rho'_{GHZ}(t) = \frac{U_{PT}^3 \rho_{GHZ}(0) U_{PT}^3}{\text{Tr}[U_{PT}^3 \rho_{GHZ}(0) U_{PT}^3]} \quad (15)$$

From this final state, the three coherences under consideration can be calculated as per the definitions given in Eqs. 8,9 and 10, and their dynamics can be studied as was done for the case of the two-qubit Bell state in the previous section.

The results of these calculations for unbroken and broken PT-symmetry regimes are presented in Figure 3. As can be seen from Figs. 3(a)-(c), in the unbroken PT-symmetry phase, all quantum coherences in tripartite

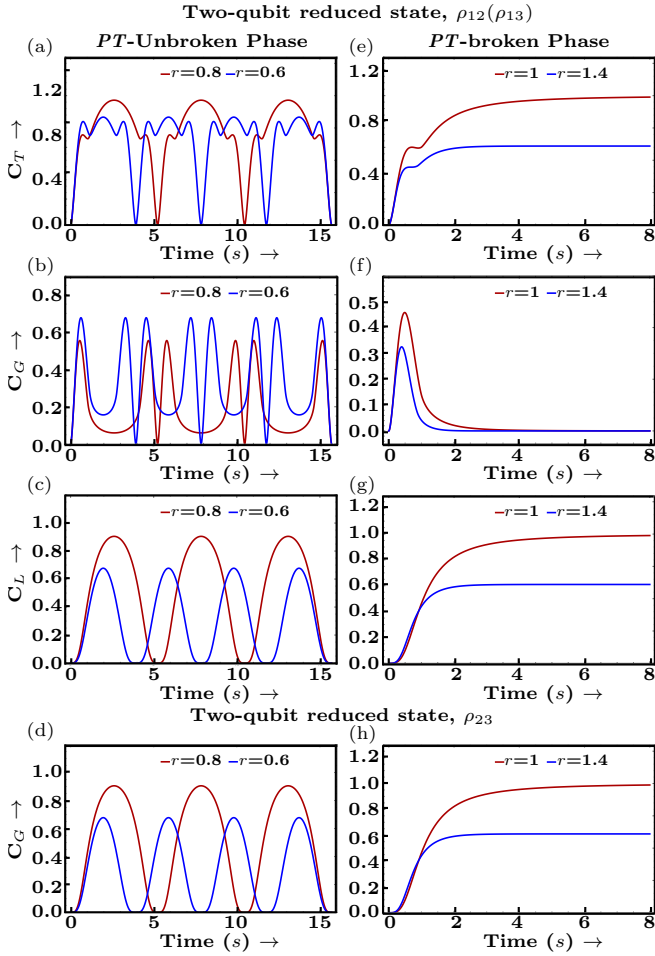


FIG. 4. Plots of the evolution of quantum coherence present in the two-qubit reduced GHZ state under different phases of PT-symmetry. (a), (b) and (c) represent the dynamics of total coherence ( $C_T$ ), global coherence ( $C_G$ ) and local coherence ( $C_L$ ) respectively, present in  $\rho_{12}(\rho_{13})$  in unbroken PT-symmetry phase ( $r = 0.6$  and  $r = 0.8$ ). (e), (f) and (g) represent the dynamics of total, global and local coherence respectively, present in  $\rho_{12}(\rho_{13})$  in a broken phase  $r = 1.4$  and at the exceptional point  $r = 1$ . (d) represents the dynamics of global coherence present in  $\rho_{23}$  in an unbroken and (h) represents the dynamics of global coherence present in  $\rho_{23}$  in the broken phase of PT-symmetry.

state show an oscillatory behavior similar to the bipartite state. As the parameter  $r$  increases and reaches the exceptional point, the transition in dynamics of total and local coherence in tripartite state can be observed, wherein the quantum coherence freezes and attains a stable value at later times. On the other hand, the dynamics of global coherence in the GHZ state is different from the Bell state, as can be observed from Fig.3(c), where the global coherence initially decays, then increases and finally freezes at later times.

Next, the dynamics of quantum coherences in three possible two-qubit reduced states ( $\rho_{ij} = \text{tr}_k(\rho_{ijk})$ , where  $i, j, k \in (1, 2, 3)$ ) of the GHZ state are studied. The re-

sults of the calculations of dynamics of various coherences for the two-qubit reduced states associated with the GHZ state are presented in Figure 4. It is observed that various quantum coherence (total, local and global) are generated in two-qubit reduced states,  $\rho_{12}$  and  $\rho_{13}$  due to the local operation of the PT-symmetric Hamiltonian on the first qubit in both unbroken and broken phase. The pattern of quantum coherence evolution in the two-qubit reduced states ( $\rho_{12}$  and  $\rho_{13}$ ) are similar to the bipartite maximally entangled Bell state as shown in Fig.4(a)-(c) and Fig.4(e)-(g). However in the two-qubit reduced state  $\rho_{23}$ , only global coherence is generated, which contributes to overall coherence. From Figs.4(d) and (h) it can be seen that the dynamics of global coherence present in  $\rho_{23}$  shows an oscillatory behavior in unbroken phase while in broken phase it initially increases and then freezes at later times.

#### D. Dynamics of coherence at the exceptional point

The results of the calculations at the exceptional point ( $r = 1$ ) for the two-qubit Bell state and the three-qubit GHZ state are depicted as contour plots in Fig. 5. The dynamics of various quantum coherences present in  $|\psi_{BS}^\alpha\rangle = \cos \alpha|00\rangle + \sin \alpha|11\rangle$  were explored at the exceptional point where  $\alpha$  is varied from 0 to  $2\pi$  i.e. the state evolves from the ground state to an excited state, passing through the maximally entangled state. From the contour plots shown in Fig.5(a)-(c), it can be observed that the total coherence stabilizes with time but the amplitude of total coherence varies with  $\alpha$ . Similar dynamics of local coherence can be observed from the contour plot, where it can be seen that the local coherence decays with time and does not depend on the  $\alpha$  value. The amplitude of the global coherence at the exceptional point first increases with time and then decays exponentially to zero. The dynamics of different quantum coherences in the broken phase are similar to the dynamics of quantum coherence observed at the exceptional point except that their amplitude decreases as the parameter  $r$  increases.

The dynamics of various types of quantum coherences present in  $|\psi_{GHZ}^\beta\rangle = \cos \beta|000\rangle + \sin \beta|111\rangle$  were investigated at the exceptional point. The parameter  $\beta$  is varied from 0 to  $2\pi$ , i.e. the state goes from the ground state  $|000\rangle$  to the excited state  $|111\rangle$ , through the maximally entangled state. The contour plots of the dynamics of the quantum coherences are shown in Figs.5(d)-(f), from where it can be observed that the total coherence freezes with time and the amplitude of the frozen coherence varies with varying  $\beta$  values of the state. Similar dynamics of global coherence can be observed from the contour plot, which shows that the global coherence freezes with time and its amplitude depends on the  $\beta$  value. The contour plot of the local coherence depicts that the local coherence stabilizes to a value 1 with time and does not depend on the  $\beta$  value. The dynamics of all quantum coherences in the broken phase are similar



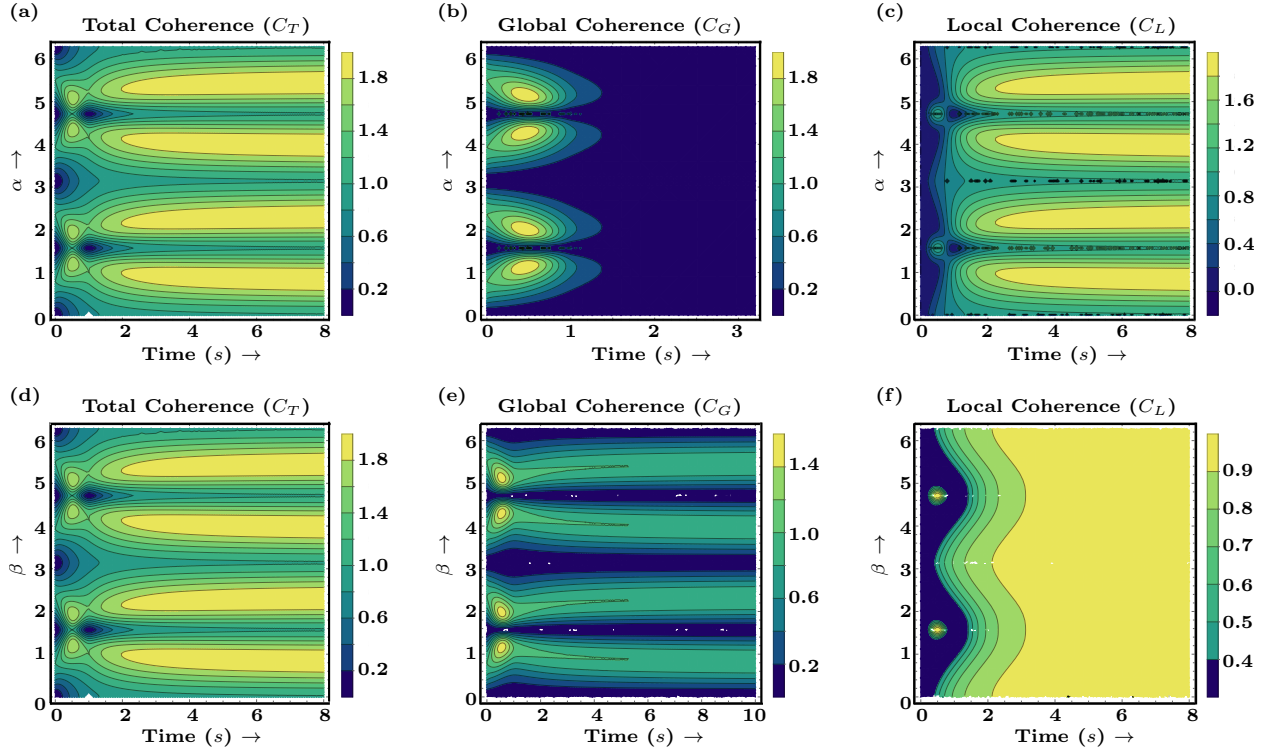


FIG. 5. Contour plots of the dynamics of (a) total coherence, (b) global coherence, and (c) local coherence, present in the state  $|\psi_{BS}^\alpha\rangle$  at the exceptional point. Contour plots of the dynamics of (d) total coherence, (e) global coherence, and (f) local coherence, present in the state  $|\psi_{GHZ}^\beta\rangle$  at the exceptional point; the angles  $\alpha$  and  $\beta$  vary from 0 to  $2\pi$  (6.28) radians.

to the dynamics of the quantum coherences observed at the exceptional point but their amplitude decreases as the parameter  $r$  increases as displayed in Figure 3(d)-(f) where panel (d) shows evolution of total coherence, panel (e) shows evolution of the global coherence and evolution of the local coherence is shown in panel (f).

#### IV. EXPERIMENTAL DEMONSTRATION OF THE DYNAMICS OF QUANTUM COHERENCE UNDER A PT-SYMMETRIC HAMILTONIAN

As discussed in Sec.II, the PT-symmetric Hamiltonian can be simulated by the dilation method using an ancillary qubit. The experimental implementation of PT-symmetric Hamiltonian on an NMR quantum processor is realized using a three-qubit system where the three spin-1/2 nuclei ( $^1\text{H}$ ,  $^{19}\text{F}$  and  $^{13}\text{C}$ ) of  $^{13}\text{C}$ -labeled diethylfluoromalonate dissolved in acetone- $\text{D}_6$ , are encoded as the first, second and third qubit respectively; the  $^1\text{H}$  and  $^{19}\text{F}$  are used as a two-qubit system while the  $^{13}\text{C}$  spin is utilized as the ancillary qubit.

The molecular structure of the three-qubit system along with tabulated system parameters and the NMR spectrum of each qubit at thermal equilibrium are shown in Fig.6(a) and Fig.6(b), respectively. The NMR Hamiltonian for a three-qubit system in a rotating frame under the weak approximation [43] is given by

$$H = - \sum_{i=1}^3 \nu_i I_z^i + \sum_{i>j,i=1}^3 J_{ij} I_z^i I_z^j \quad (16)$$

where  $i, j = 1, 2$  and  $3$  label the nuclear spin,  $\nu_i$  is the chemical shift of the  $i$ th spin,  $J_{ij}$  represents the scalar spin-spin coupling strength and  $I_z^i$  is the  $z$  component of the spin angular momentum operator for the  $i^{\text{th}}$  spin. The three-qubit system was initialized into a pseudopure state (PPS)  $|000\rangle$  using the spatial averaging technique [44, 45], with the density  $\rho_{000}$  given by

$$\rho_{000} = \frac{(1-\epsilon)}{8} I + \epsilon |000\rangle\langle 000| \quad (17)$$

where  $\epsilon \sim 10^{-5}$  represents the spin polarization at room temperature and  $I$  is the  $8 \times 8$  identity operator. The NMR spectrum of the three-qubit PPS is shown in Fig.6(c). The experimentally prepared PPS was tomographed and its fidelity was computed to be  $0.9857 \pm 0.0001$  using the Uhlmann-Jozsa fidelity measure [46, 47].

The density matrix of the initial state was reconstructed using least square constrained convex optimization method [48] by performing full quantum state tomography using a set of seven preparatory pulses  $\{III, XXX, IYY, XYX, YII, XXY, IYY\}$  where  $I$  represents 'no-operation' and  $X(Y)$  is the local  $\pi/2$  unitary operator with phases  $x(y)$  and local operations

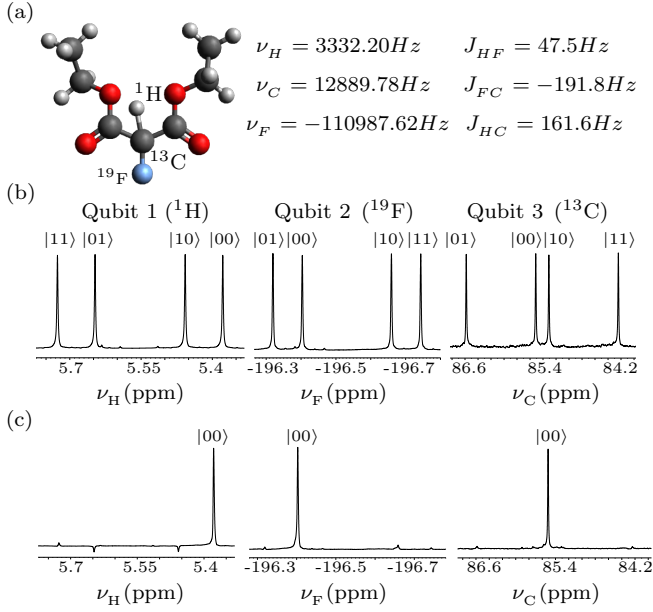


FIG. 6. (a) Molecular structure of  $^{13}\text{C}$ -labeled diethylfluoromalonate with the three qubits encoded as  $^1\text{H}$ ,  $^{19}\text{F}$  and  $^{13}\text{C}$  and the system parameters given alongside. (b) NMR spectrum of thermal equilibrium state obtained after a  $\pi/2$  readout pulse. (c) NMR spectrum of the pseudopure state. Each resonance peak is labeled in the logical basis and the horizontal scale of each spectrum denotes the chemical shift in ppm.

are achieved using spin-selective  $\pi/2$  radiofrequency (rf) pulses. All experiments were performed at room temperature 293K on a Bruker Avance-III 600 MHz FT-NMR spectrometer equipped with a QXI probe.

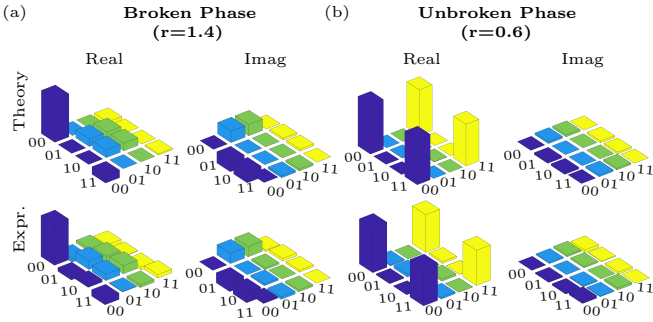


FIG. 7. Real (left) and imaginary (right) parts of the theoretically expected and experimentally reconstructed density matrix of the Bell State after implementation of the PT-symmetric Hamiltonian at time  $t = 4\text{s}$  under (a) a broken phase at non-hermiticity strength  $r=1.4$  and (b) an unbroken phase at non-hermiticity strength  $r=0.6$ .

The quantum circuit to implement PT-symmetric Hamiltonian is shown in Fig.1(a). The first block creates the maximally entangled bipartite state (Bell State,  $\rho_{BS} \otimes \rho_0$ ) on two qubits ( $\rho_{BS}$ ) and the third qubit ( $\rho_0$ ) is utilized as an ancillary qubit. The next block of the

circuit implements a PT-symmetric Hamiltonian on the first qubit of the two-qubit state using an ancillary qubit where the parameter  $r$ , and the time period ( $t$ ) are varied by  $\theta$  and  $\phi$  as given in Eq. [4] and Eq. [7] respectively;  $\theta$  is controlled by the operator  $V$  and  $\phi$  by the operator controlled- $U_1$ . All quantum gates were implemented using rf-pulses and free evolution under the system Hamiltonian. Local rotations were implemented by spin-selective pulses with different phases; the durations of  $\pi/2$  pulses for  $^1\text{H}$ ,  $^{19}\text{F}$  and  $^{13}\text{C}$  nuclei were  $9.38 \mu\text{s}$ ,  $21.8 \mu\text{s}$  and  $15.1 \mu\text{s}$  at power levels of 18.14 W, 42.27 W and 179.47 W, respectively.

The NMR pulse sequence used to experimentally prepare a maximally entangled bipartite state is shown in Fig.1(b). The fidelity of the initial state ( $\rho_{BS} \otimes \rho_0$ ) created was found to be  $0.9745 \pm 0.0102$ . The method to simulate the PT-symmetric Hamiltonian is described in Sec.II, where  $\theta$  and  $\phi$  control the degree of non-hermiticity  $r$  and the time point of evolution  $t$ . We experimentally simulated the PT-symmetric Hamiltonian by choosing parameters  $r = 0.6$  and  $r = 1.4$  corresponding to unbroken and broken phase respectively, which was implemented on the first qubit of the bipartite state, using the third qubit as an ancillary qubit. The parameter  $r$  was fixed depending on different phases of PT-symmetry, and the state was allowed to evolve by increasing the time period  $t$  and accordingly varying  $\theta$  and  $\phi$ . Each state was tomographed at different time points after implementing the PT-symmetric Hamiltonian in both the unbroken and broken phase. The final density matrices of the two qubit-Bell states were reconstructed by measuring in the  $|0\rangle$  subspace of the ancillary qubit, where only three tomographic pulses ( $III$ ,  $IYY$ ,  $YII$ ) were required to reconstruct the entire density matrix. A representative tomograph of the experimentally reconstructed density matrix of the Bell state after the implementation of the PT-symmetric Hamiltonian in two different phases (unbroken phase at  $r = 0.6$  and broken phase at  $r = 1.4$ ) of PT-symmetry at time  $t = 4\text{s}$  is shown in Fig.7.

A single qubit coherence flow in PT-symmetric and anti-PT-symmetric systems was demonstrated experimentally using an optical setup and it was observed that coherence flow oscillates back and forth in the unbroken PT-symmetric and anti-PT-symmetric regimes while in broken phase, coherence flow attains a stable value in both PT-symmetric and anti-symmetric systems [24]. We investigated the dynamics of quantum coherence (total, local and global coherence) in the maximally entangled (Bell) state, when one qubit of the Bell state is acted upon by the PT-symmetric Hamiltonian at  $r = 0.6$  (unbroken phase) and at  $r = 1.4$  (broken phase). The results are plotted in Fig.8 where (a), (b) and (c) depict the dynamics of various types of quantum coherences in the unbroken phase and (d), (e) and (f) depict the dynamics of various types of quantum coherence in the broken phase. Similar patterns of coherence dynamics are observed as in the case of the optics setup [24]. Our results in Fig.8 (a)-(c) show that in the Bell state, the total,

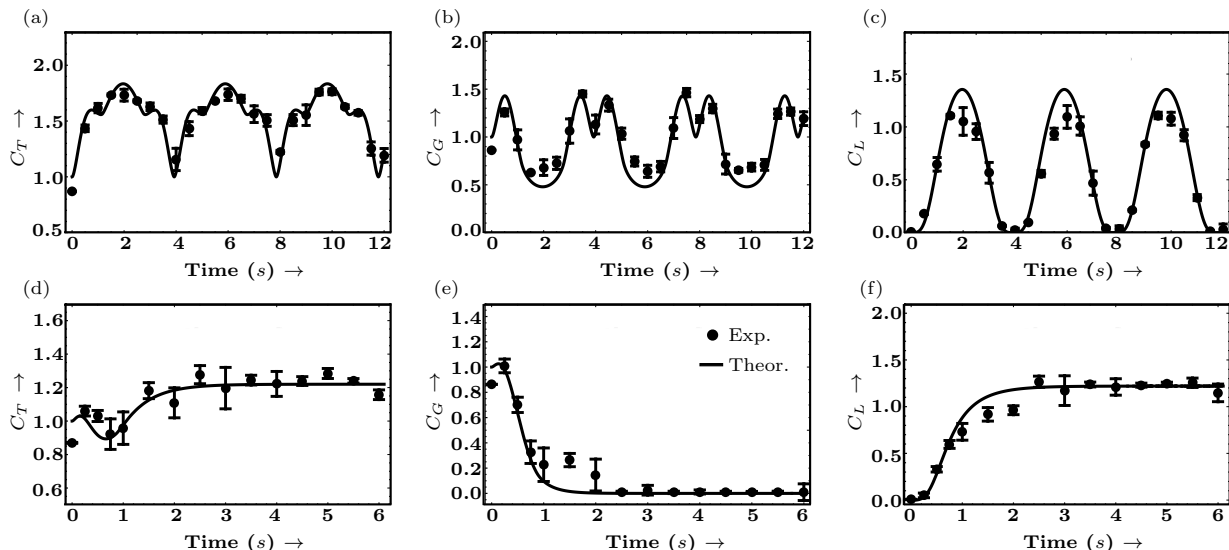


FIG. 8. Dynamics of quantum coherence present in the two-qubit maximally entangled Bell State under a  $PT$ -Symmetric Hamiltonian. Plots in (a), (b) and (c) represent the dynamics of the total coherence ( $C_T$ ), global coherence ( $C_G$ ) and local coherence ( $C_L$ ) respectively, in the unbroken phase of  $PT$ -Symmetry ( $r = 0.6$ ). (d), (e) and (f) represent the dynamics of the total coherence ( $C_T$ ), global coherence ( $C_G$ ) and local coherence ( $C_L$ ) respectively, in the broken phase of  $PT$ -Symmetry ( $r = 1.4$ ). The black lines are the theoretical curves (Theor.) and the black filled circles are the experimental points (Exp.).

local and global coherences oscillate with time in the unbroken phase ( $r = 0.6$ ) while the amplitudes are different for various quantum coherences. Another interesting feature of local coherence generation is observed that it oscillates with time, and is not present in the initial Bell state. In the broken phase ( $r = 1.4$ ), the total coherence initially increases and then freezes at later times. Similarly, the results of Fig.8(c) indicate that the local coherence, which is not present initially in the Bell state, is created and increases under the broken phase of  $PT$ -symmetry and freezes at later times. Fig.8 (b) shows that the global coherence initially increases and then exponentially decays with time. Our experimental results match well with the theoretically predicted behavior of quantum coherence, within experimental errors.

Similar patterns of information flow have been observed in NMR in a single-qubit system where information flow oscillates in the broken phase while it decays with time in the unbroken phase of anti- $PT$ -symmetry [12]. A similar freezing pattern of quantum coherence has also been observed in a two-qubit subsystem of a three-qubit GHZ state under the  $PT$ -symmetric Hamiltonian using nuclear spins, where it was observed that entropy and entanglement stabilize to a certain value [13].

## V. CONCLUSION

We have theoretically investigated the dynamics of quantum coherence (total, global and local coherence) present in maximally entangled bipartite and tripartite

states in both the unbroken and the broken phase of  $PT$ -symmetry and at an exceptional point when one qubit is acted upon by the local  $PT$ -symmetric Hamiltonian. Our results show that the different types of quantum coherence oscillate in the unbroken phase of  $PT$ -symmetry. In the broken phase of  $PT$ -symmetry and at the exceptional point, the total and local coherence first increase and then attain a stable value over time in both the maximally entangled bipartite and tripartite states. The global coherence decays exponentially in the bipartite state but freezes over time in the tripartite state. Our results indicate that quantum coherence behaves differently under  $PT$ -symmetry, when the dimensionality of the quantum system is increased. The dynamics of quantum coherence present in the maximally entangled bipartite state was experimentally verified by implementing the  $PT$ -symmetric Hamiltonian on an NMR quantum processor. Our work sheds some light on the effect of the  $PT$ -symmetric Hamiltonian on quantum coherences in a multipartite system. Our results can help in gaining an understanding of the effects of the  $PT$ -symmetric Hamiltonian in quantum thermodynamics and in quantum information processing[49, 50].

## ACKNOWLEDGMENTS

All the experiments were performed on a Bruker Avance-III 600 MHz FT-NMR spectrometer at the NMR Research Facility of IISER Mohali. A. acknowledges financial support from DST/ICPS/QuST/Theme-1/2019/Q-68. K.D. acknowledges financial support from DST/ICPS/QuST/Theme-2/2019/Q-74.



- 
- [1] C. M. Bender and S. Boettcher, Phys. Rev. Lett. **80**, 5243 (1998).
- [2] C. M. Bender, Reports on Progress in Physics **70**, 947 (2007).
- [3] Ş. K. Özdemir, S. Rotter, F. Nori, and L. Yang, Nat. Mater. **18**, 783 (2019).
- [4] R. El-Ganainy, K. G. Makris, M. Khajavikhan, Z. H. Musslimani, S. Rotter, and D. N. Christodoulides, Nat. Phys. **14**, 11 (2018).
- [5] J. Li, A. K. Harter, J. Liu, L. de Melo, Y. N. Joglekar, and L. Luo, Nat. Commun. **10**, 855 (2019).
- [6] F. Quijandría, U. Naether, S. K. Özdemir, F. Nori, and D. Zueco, Phys. Rev. A **97**, 053846 (2018).
- [7] M. Naghiloo, M. Abbasi, Y. N. Joglekar, and K. W. Murch, Nat. Phys. **15**, 1232 (2019).
- [8] A. Pick, S. Silberstein, N. Moiseyev, and N. Bar-Gill, Phys. Rev. Research **1**, 013015 (2019).
- [9] Y. Wu, W. Liu, J. Geng, X. Song, X. Ye, C.-K. Duan, X. Rong, and J. Du, Science **364**, 878 (2019).
- [10] C. E. Rüter, K. G. Makris, R. El-Ganainy, D. N. Christodoulides, M. Segev, and D. Kip, Nat. Phys. **6**, 192 (2010).
- [11] F. Klauck, L. Teuber, M. Ornigotti, M. Heinrich, S. Scheel, and A. Szameit, Nat. Photon. **13**, 883 (2019).
- [12] J. Wen, C. Zheng, X. Kong, S. Wei, T. Xin, and G. Long, Phys. Rev. A **99**, 062122 (2019).
- [13] J. Wen, G. Qin, C. Zheng, S. Wei, X. Kong, T. Xin, and G. Long, npj Quantum Information **6**, 28 (2020).
- [14] S.-L. Chen, G.-Y. Chen, and Y.-N. Chen, Phys. Rev. A **90**, 054301 (2014).
- [15] Y.-Y. Wang and M.-F. Fang, Quant. Inf. Proc. **17**, 208 (2018).
- [16] Y.-C. Lee, M.-H. Hsieh, S. T. Flammia, and R.-K. Lee, Phys. Rev. Lett. **112**, 130404 (2014).
- [17] J.-S. Tang, Y.-T. Wang, S. Yu, D.-Y. He, J.-S. Xu, B.-H. Liu, G. Chen, Y.-N. Sun, K. Sun, Y.-J. Han, C.-F. Li, and G.-C. Guo, Nat. Photon. **10**, 642 (2016).
- [18] U. Günther and B. F. Samsonov, Phys. Rev. Lett. **101**, 230404 (2008).
- [19] C. M. Bender, D. C. Brody, H. F. Jones, and B. K. Meister, Phys. Rev. Lett. **98**, 040403 (2007).
- [20] K. Kawabata, Y. Ashida, and M. Ueda, Phys. Rev. Lett. **119**, 190401 (2017).
- [21] L. Xiao, K. Wang, X. Zhan, Z. Bian, K. Kawabata, M. Ueda, W. Yi, and P. Xue, Phys. Rev. Lett. **123**, 230401 (2019).
- [22] J. Naikoo, S. Kumari, S. Banerjee, and A. K. Pan, J. Phys. A: Math. Ther. **54**, 275303 (2021).
- [23] W.-C. Wang, Y.-L. Zhou, H.-L. Zhang, J. Zhang, M.-C. Zhang, Y. Xie, C.-W. Wu, T. Chen, B.-Q. Ou, W. Wu, H. Jing, and P.-X. Chen, Phys. Rev. A **103**, L020201 (2021).
- [24] Y.-L. Fang, J.-L. Zhao, Y. Zhang, D.-X. Chen, Q.-C. Wu, Y.-H. Zhou, C.-P. Yang, and F. Nori, Commun. Phys. **4**, 223 (2021).
- [25] V. Narasimhachar and G. Gour, Nat. Commun. **6**, 7689 (2015).
- [26] M. Lostaglio, K. Korzekwa, D. Jennings, and T. Rudolph, Phys. Rev. X **5**, 021001 (2015).
- [27] K. Korzekwa, M. Lostaglio, J. Oppenheim, and D. Jennings, New J. Phys. **18**, 023045 (2016).
- [28] A. Ishizaki, T. R. Calhoun, G. S. Schlau-Cohen, and G. R. Fleming, Phys. Chem. Chem. Phys. **12**, 7319 (2010).
- [29] G. S. Engel, T. R. Calhoun, E. L. Read, T.-K. Ahn, T. Mančal, Y.-C. Cheng, R. E. Blankenship, and G. R. Fleming, Nature **446**, 782 (2007).
- [30] N. Lambert, Y.-N. Chen, Y.-C. Cheng, C.-M. Li, G.-Y. Chen, and F. Nori, Nat. Phys. **9**, 10 (2013).
- [31] O. Karlström, H. Linke, G. Karlström, and A. Wacker, Phys. Rev. B **84**, 113415 (2011).
- [32] A. Streltsov, G. Adesso, and M. B. Plenio, Rev. Mod. Phys. **89**, 041003 (2017).
- [33] T. Baumgratz, M. Cramer, and M. B. Plenio, Phys. Rev. Lett. **113**, 140401 (2014).
- [34] V. Le Duc, M. Nowotarski, and J. K. Kalaga, Symmetry **13**, 10.3390/sym13020203 (2021).
- [35] J. Wen, C. Zheng, Z. Ye, T. Xin, and G. Long, Phys. Rev. Research **3**, 013256 (2021).
- [36] A. E. Rastegin, Phys. Rev. A **93**, 032136 (2016).
- [37] S. Rana, P. Parashar, and M. Lewenstein, Phys. Rev. A **93**, 012110 (2016).
- [38] L.-H. Shao, Z. Xi, H. Fan, and Y. Li, Phys. Rev. A **91**, 042120 (2015).
- [39] H. Cao, C. Radhakrishnan, M. Su, M. M. Ali, C. Zhang, Y.-F. Huang, T. Byrnes, C.-F. Li, and G.-C. Guo, Phys. Rev. A **102**, 012403 (2020).
- [40] C. Radhakrishnan, M. Parthasarathy, S. Jambulingam, and T. Byrnes, Phys. Rev. Lett. **116**, 150504 (2016).
- [41] C. Zheng, Europhys. Lett. **123**, 40002 (2018).
- [42] L. Gui-Lu, Comm. in Theor. Phys **45**, 825 (2006).
- [43] R. R. Ernst, G. Bodenhausen, and A. Wokaun, *Principles of NMR in One and Two Dimensions* (Clarendon Press, 1990).
- [44] D. G. Cory, M. D. Price, and T. F. Havel, Physica D: Nonlinear Phenomena **120**, 82 (1998).
- [45] A. Mitra, K. Sivapriya, and A. Kumar, J. Magn. Reson. **187**, 306 (2007).
- [46] A. Uhlmann, Rep. Math. Phys. **9**, 273 (1976).
- [47] R. Jozsa, J. Mod. Optics **41**, 2315 (1994).
- [48] A. Gaikwad, Arvind, and K. Dorai, Quant. Inf. Proc. **20**, 19 (2021).
- [49] B.-B. Wei, Phys. Rev. E **97**, 012114 (2018).
- [50] S. Deffner and A. Saxena, Phys. Rev. Lett. **114**, 150601 (2015).